Science Advances

AAAS

advances.sciencemag.org/cgi/content/full/4/3/eaar3031/DC1

Supplementary Materials for

Molecular engineered conjugated polymer with high thermal conductivity

Yanfei Xu, Xiaoxue Wang, Jiawei Zhou, Bai Song, Zhang Jiang, Elizabeth M. Y. Lee, Samuel Huberman, Karen K. Gleason, Gang Chen

Published 30 March 2018, *Sci. Adv.* **4**, eaar3031 (2018)
DOI: 10.1126/sciadv.aar3031

The PDF file includes:

section S1. Materials and Methods

1.1 oCVD experiment

oCVD is a one-step process where the monomer and the oxidant are introduced simultaneously in the vapor phase in a vacuum chamber. The process was conducted in a custom-built reactor reported in previous literature (*24*, *25*, *36*, *37*) (fig. S1a).

1.2 Substrate preparation

The oCVD P3HT samples were grown on glass and Si (100) substrates with a native silicon oxide layer. In order to enhance the adhesion of P3HT on silicon substrates, the silane grafting technique was applied (*36*): silicon substrates were treated with oxygen plasma (29.6W, 30 min) and then exposed to trichlorovinylsilane (TCVS-$C_2H_3SiCl_3$) while being heated to ~75°C to form the vinyl terminated surface for further P3HT linking.

1.3 Equipment setup

The oCVD chamber was cubic with inner side length of 30 cm. The oxidant ($FeCl_3$, reagent grade > 97%, anhydrous, SigmaAldrich) was heated with a crucible in a heating furnace (LUXEL RADAK 1), which was placed on the back of the reactor inside the chamber. The glass (or silicon) substrates were placed on the front glass window of the reactor chamber. The distance between the substrate and the oxidant crucible is ~30 cm. The temperature of the substrates was monitored with a thermocouple placed near the substrate inside the chamber, and controlled by cryogenic gel packet placed on the outer side of the glass window. The monomer (3-hexylthiophene, reagent grade ≥ 99%, SigmaAldrich), was introduced with a heated glass jar (MDC Vaccum Products, LLC.) and through a heated tube. Both of the jar and tube are connected to the chamber from outside. The flowrate of the monomer was controlled by a needle valve (SS-4BMW-VCR, Swagelok). And the flowrate of the $FeCl_3$ was controlled by a hot tungsten wire.

1.4 Experimental conditions

During the oCVD growth, the pressure of the chamber was controlled at 4 mTorr. The monomer (3-hexylthiophene) was heated at 140°C, and the oxidant ($FeCl_3$) was heated from 100°C to ~160°C at a constant heating rate of 1.5°C/min. In order to control the oxidant amount, a glass tube with a heating tungsten wire (heated with ~2.3 A × 2.3 V) was added on top of the crucible to trap the excessive oxidant. The flow rate of the monomer was controlled at ~1.2 sccm with opening the Swagelok needle valve for 4 turns, and the deposition time was ~40 minutes. The outer wall of the reactor chamber was heated constantly to 200°C in order to avoid unnecessary monomer adsorption. After the deposition, the P3HT/$FeCl_3$ films were rinsed with pure methanol at room temperature for 1 min in order to remove the residue and to fully de-dope P3HT. After the rinsing process, the P3HT films were dried with blow of compressed air immediately.

section S2. Characterizations

The molecular weight was determined by gel permeation chromatography (GPC, table S1), 45°C and 85°C-grown P3HT were eluted with tetrahydrofuran at 1.0 mL/min and measured relative to a polystyrene calibration curve. ^{1}H NMR (nuclear magnetic resonance) spectra of 45°C and 85°C-grown P3HT are shown in fig. S4. The specific heat was analyzed by differential scanning calorimetry measurement (DSC, fig. S5a). The P3HT structure was further characterized by Raman spectroscopy (fig. S5b and S5c).

2.1 Thickness measurement

The sample thickness was measured with a Veeco Dektak 150 profilometer. The thickness of 45°C and 85°C-grown P3HT grown by oCVD ranged from 100 nm to 210 nm. Representative P3HT thickness is shown in fig. S3e.

2.2 UV-vis-NIR spectroscopy measurement

UV-vis-NIR optical absorption was investigated by the Cary Series UV-vis-NIR spectrophotometer (Agilent Technologies).

Photoluminescence spectroscopy: samples deposited on glass slides were excited by a 365 nm, fiber-coupled LED for photoluminescence measurements (Thorlabs). Photoluminescence spectra were collected in air using an Avantes fiber-optic spectrometer with an integration time of 100 ms, and each spectrum was averaged over 10 scans.

2.3 Raman spectroscopy

Raman spectroscopy was collected on a HORIBA Labram HR Evolution spectrometer, laser wavelength was 532 nm.

2.4 Differential scanning calorimetry measurement

DSC measurements were performed at atmospheric pressure by using a TA DSC RCS1-3277 instruments. The calorimeter was calibrated with standard sapphire. The melting behavior of crystals was investigated through a heating scan with a heating rate of 5 K/min at N_2 atmosphere.

2.5 Density measurement

The density of the P3HT film was 0.9 g/cm^3 for both 45°C-grown and 85°C-grown P3HT. We observed that the P3HT films float in water (ρ=1 g/cm^3) while sink in methanol (ρ=0.793 g/cm^3). Therefore, we measured the density of the water-methanol mixtures in which the P3HT films suspend after being stabilized for 20 min, and use this density as the density of the P3HT films.

2.6 Synchrotron X-ray scattering measurement

Synchrotron GIWAXS measurements were carried out at beamline 8-ID-E of the Advanced Photon Source (APS), Argonne National Laboratory, United States. The wavelength λ of the X-ray beam was 1.15 Å (10.82 keV). All samples were mounted in a vacuum chamber to reduce air scattering background. An incident angle below the critical angle of the total reflection of the

silicon substrate (~0.165 degree) was used to enhance the scattering signals. A Pilatus 1M area detector mounted 228 mm downstream of the sample was used to collect all GIWAXS data.

2.7 Thermal conductivity measurement

Time-domain thermoreflectance method was employed to measure the thermal conductivity of the polymer film (fig. S6) (*28*, *29*). A pump laser beam first heats up the sample surface. As the heat propagates into the material, the surface temperature decreases. A delayed probe laser beam is then reflected from the sample into the detector. The reflectance of the probe beam changes with the surface temperature (governed by the thermoreflectance coefficient), and thus records the surface temperature decay as time. A thin film of aluminum (Al, ~100 nm) was deposited onto the P3HT film for larger signal because aluminum has large thermoreflectance coefficient. Pump beam has wavelength at 400 nm while probe beam has wavelength at 800 nm. The measured thermoreflectance signals are then fitted to a standard two-dimensional, three-layer heat conduction model considering the aluminum transducer, the polymer film and the interface in-between. Details of the thermal modeling can be found in past work (*29*). We note that we have carefully checked the fitting curve agrees well with both the amplitude and phase signals from the measurement (fig. S8). We also note that multiple pump modulation frequencies (3 MHz, 6 MHz and 9MHz) were used, and the thermal conductivity at a fixed temperature for a given sample is taken to be the average of different measurements.

2.8 Notes on TDTR experimental sensitivity and uncertainty

Here we provide a detailed analysis of the experimental sensitivity and uncertainty, to justify our obtained results from the TDTR measurements.

The sensitivity (*S*) can be defined as the logarithmic derivative of an experimental observable (say *A*) with respect to a fitting parameter (say *x*) (*38*), namely $S_x = \left|\frac{\partial lnA}{\partial lnx}\right|$. This is a commonly used approach to evaluate how sensitive a measured signal is to a small variation in different fitting parameters. Because our sample is grown on a substrate (glass and silicon, fig S6), our fitting could potentially depend on the following parameters: aluminum thickness, sample thermal conductivity, sample specific heat, first interface conductance (between aluminum and sample), second interface conductance (between sample and substrate), and substrate thermal conductivity. The aluminum thickness is accurately determined by profilometer measurement. For the 45°C-grown P3HT on glass substrate, we measured an aluminum thickness of 107 nm, which is also confirmed by measuring the roundtrip time of a laser-excited acoustic pulse from the metal surface to the metal-P3HT interface (~102 nm). While the former is used in our fitting, we note that the variation of the fitting result is less than 10% if the latter is chosen as the metal thickness. The specific heat is measured via differential scanning calorimetry, as stated above. For the four remaining parameters, we performed a sensitivity analysis as shown in fig. S9 (all the parameters chosen represent our experimental condition as clarified in the figure caption). This plot shows that the fitting is not at all sensitive to the second interface and the substrate in our condition. Therefore, a three-layer model including only the aluminum and the sample is

well justified, which is used to obtain the thermal conductivity values throughout the work. In fact, we have also performed the fitting with the substrate taken into account, which yielded identical results for the sample thermal conductivity.

When fitting the two parameters – sample thermal conductivity (k) and interface conductance between aluminum and sample (G) – we are also faced with potential coupling issues (between these two). This means that several (k, G) pairs could potentially be equally good in fitting the experimental curve when there is certain noise in the data. In fig. S10, we map out the fitting residues (a measure of how closely the fitted curve matches the experimental curve) on the G-k plane, from which one can get a sense of how a different interface conductance might affect the fitted sample thermal conductivity (*39*). The contour line indicates those (k, G) pairs whose fitting would yield residue value two times the minimum residue achieved by an optimized (k, G) pair. A small residual range indicates that there is small fitting uncertainty. We specifically tested the residue for the better sample (fabricated at 45^{o}C with high thermal conductivity) at all temperatures measured. It is clear from fig. S10 that the extension of the residual contour is small, in particular along the sample thermal conductivity dimension, which means that thermal conductivity can be relatively well determined. The trend of the thermal conductivity also agrees with the Fig. 2 in the main manuscript. This therefore justifies our measured thermal conductivity values.

table S1. Molecular weight and molecular weight distribution.

	Mn	*Mw*	*Distribution*
45°C-grown P3HT	7655	16650	2.17
85°C-grown P3HT	3520	5000	1.42

a

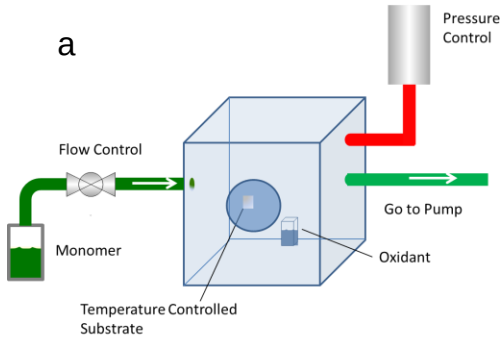

b

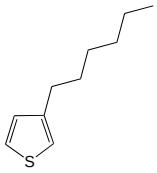

c

(1) Oxidation of 3HT to from cation radical

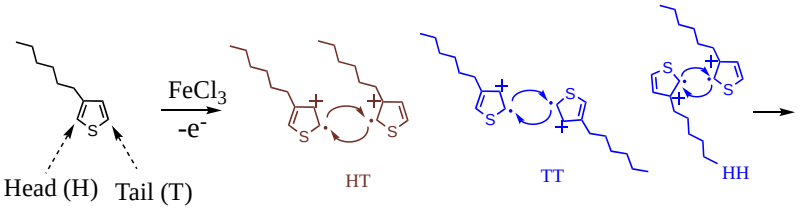

(2) Dimerization of cation radical

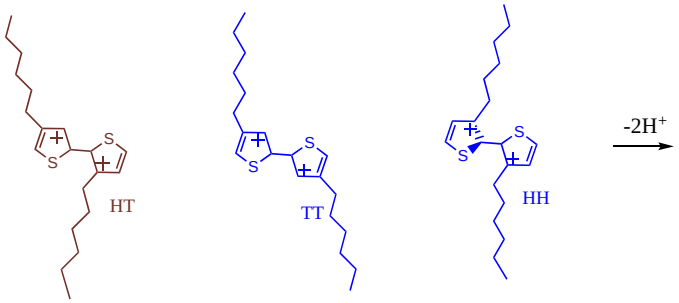

(3) Deprotonation to form conjugation

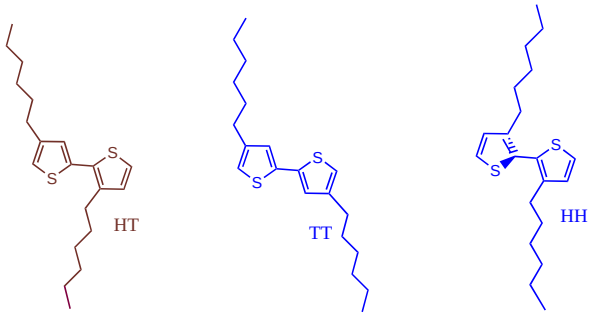

(4) Step-growth polymerization

(i) Oxidation of 3HT to from cation radical

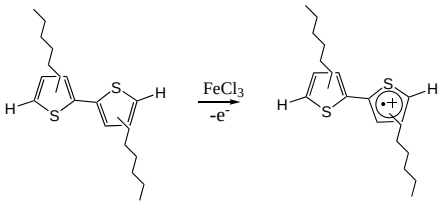

(ii) 1) Dimerization of cation radical and 2) deprotonation to form conjugation

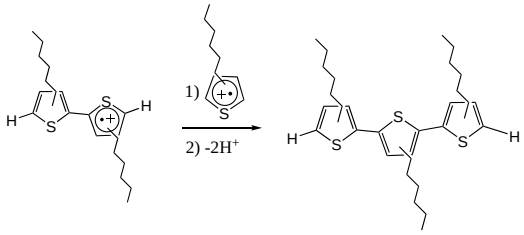

(iii) 1) Dimerization of cation radical and 2) deprotonation to form conjugation

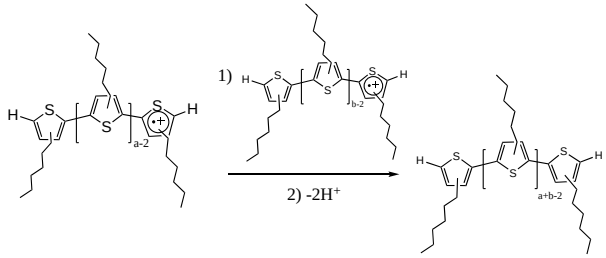

(5) Simultaneous chlorine doping of polymer backbone

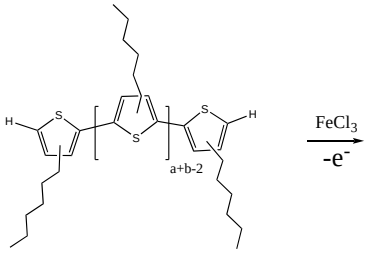

Doped polymer backbone

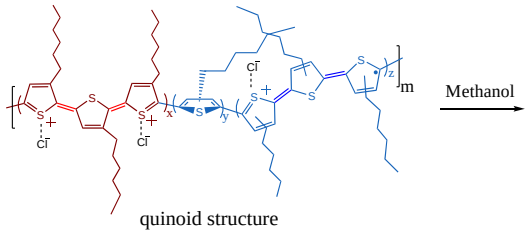

quinoid structure

(6) Dedoping of polymer backbone

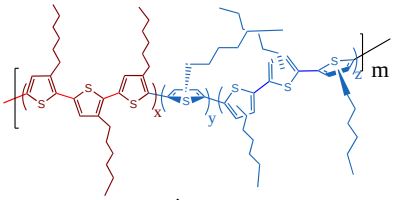

aromatic structure

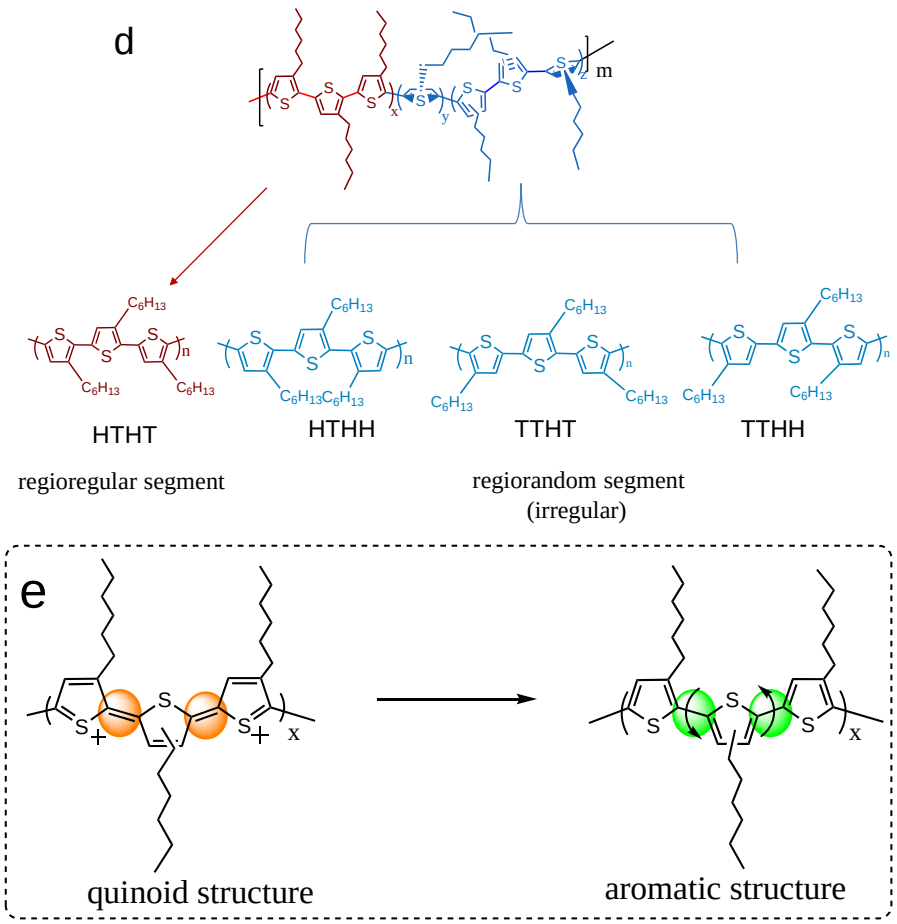

fig. S1. Synthesis mechanism and molecular structure. (**a**) Schematic of oCVD reactor for P3HT synthesis. A glass tube with a heating tungsten wire (heated with ~2.3 A × 2.3 V) was added on top of the crucible to trap the excessive oxidant. The temperature of the substrates was controlled by a cryogenic bag outside of the window, and was monitored by a thermocouple placed next to the substrate (glass and silicon). (**b**) Monomer 3-hexylthiophene**.** (**c**) Step-growth polymerization process (1) oxidation of 3HT to from cation radical; (2) dimerization of cation radical; the 3-hexyl side chain in a thiophene ring can be incorporated into a polymer chain by head-to-tail (HT, regioregular couplings), tail-to-tail (TT, regiorandom couplings) and head-to-head (HH, regiorandom couplings) oxidative coupling polymerization. (3) Deprotonation to form conjugation; (4) step growth polymerization process; (5) simultaneous chlorine doping of polymer backbone; (6) de-doping of P3HT backbone by methanol. During the step-growth polymerization via bottom-up oCVD approach, the synthesized backbones are heavily oxidative doped by the excessive oxidants, and form the quinoid structure (fig. S1e left), show high planarity, and have potentially suppressed the head-to-head coupling polymerization due to the steric interference (fig. S1d). Inherited from quinoid structure, the aromatic chain is obtained by de-doping the quinoid structures by rinsing treatment with methanol, which has potentially suppressed head-to-head (twisted) segment. Low percentage of monomers adopting a head-to-head configuration is desired for efficient phonon transport. (**d**) Possible regiochemical coupling in P3HT. (**e**) Schematic illustration of quinoid and aromatic structure.

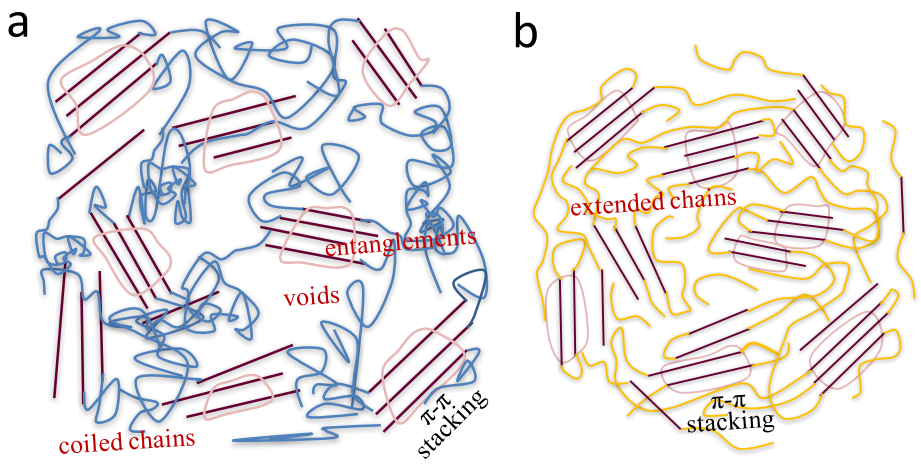

fig. S2. Cartoon for P3HT backbone conformation. (**a**) Randomly coiled and entangled polymer chains with π-π stacking regions. (**b**) Extended chains in 45°C-grown P3HT with π-π stacking regions.

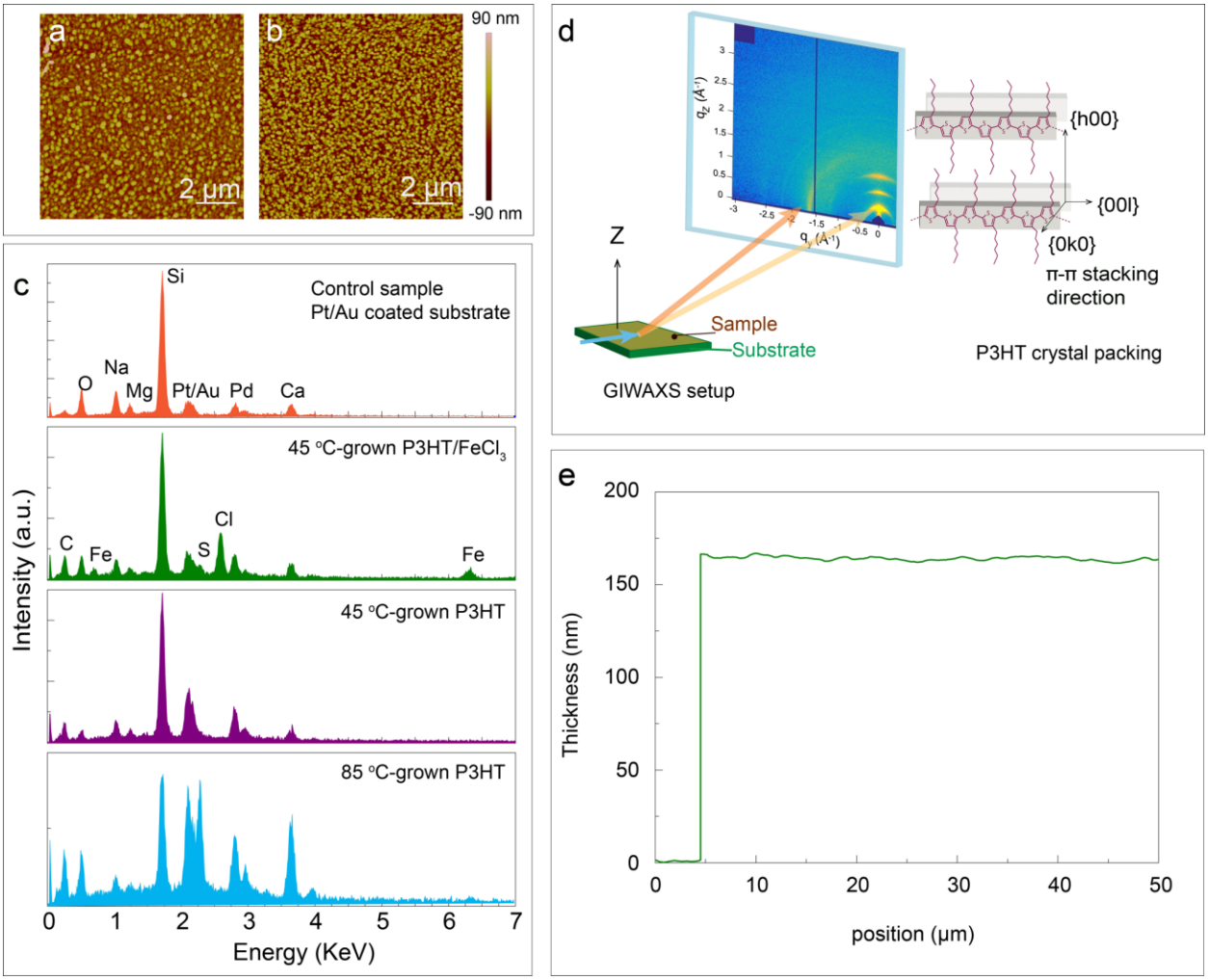

fig. S3. Morphology, thickness, elemental analysis, and x-ray scattering characterization. (**a**) Tapping-mode AFM image for nanorod-like 45°C-grown P3HT/$FeCl_3$ on glass substrate, 10 minute's oxidative coupling polymerization. (**b**) Tapping-mode AFM image for 85°C-grown P3HT/$FeCl_3$ on glass substrate, 10 minute's oxidative coupling polymerization. (**c**) Elemental analysis by energy dispersive X-ray spectroscopy. 45°C and 85°C-grown P3HT demonstrate the signature elements (S and C) of P3HT, no residue left on the P3HT after the de-doping process. (**d**) Structural characterization by synchrotron X-ray scattering. Illustration of the GIWAXS setup and P3HT crystal packing. (**e**) Representative film thickness of 45°C-grown P3HT, as measured with a stylus profilometer.

a

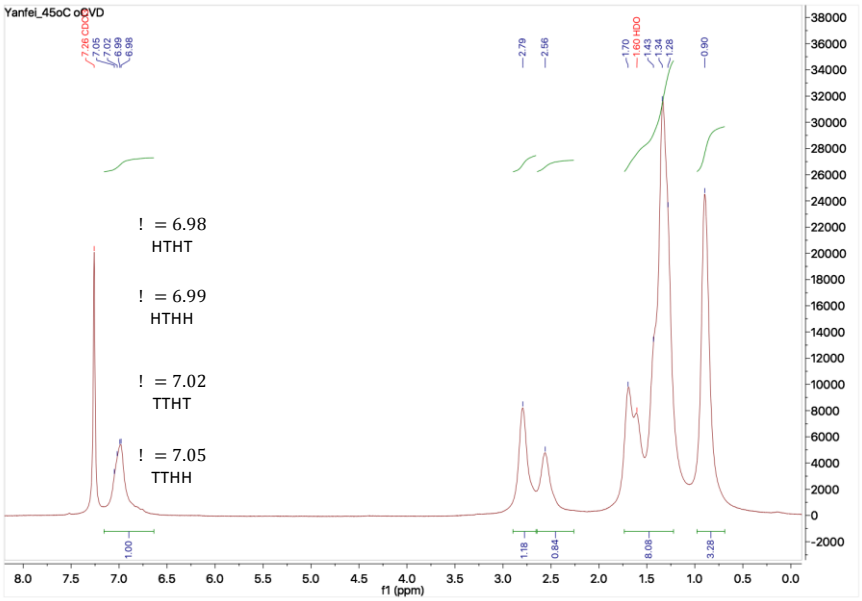

b

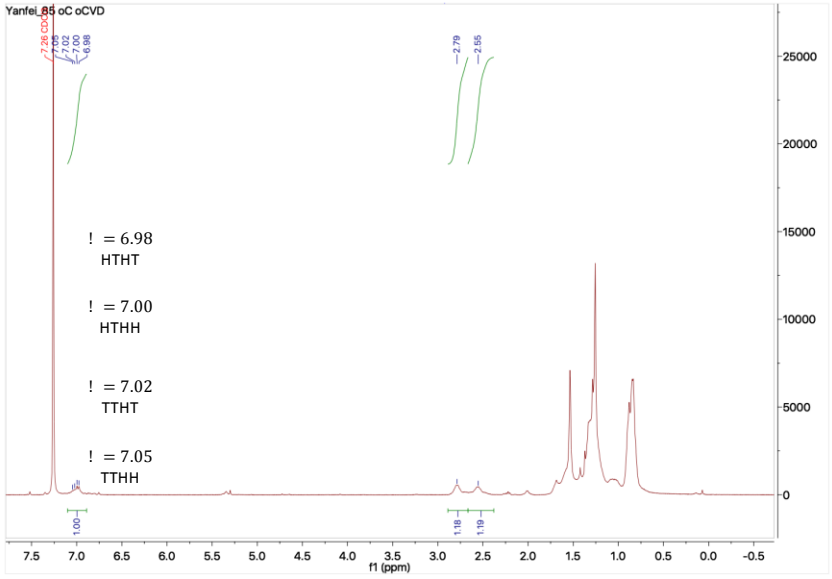

fig. S4. NMR spectroscopy. (**a**) 45°C-grown P3HT, ^{1}H NMR ($CDCl_3$): δ 0.50-1.00 (3H, -CH_3), 1.00- 2.00 (8H, -(CH_2)$_4$-), 2.33-3.00 (2H, ring-CH_2 from both HT coupling and non-HT-coupling). 6.60-7.16 (1H, ring proton). The ratio of regioregular to regiorandom couplings is 3:2 (fig. S1d), which is estimated by the relative integration of the HT couplings (δ = 2.79 ppm) and non-HT couplings (δ = 2.56 ppm) (*40*). (**b**) 85°C-grown P3HT, ^{1}H NMR ($CDCl_3$): δ 2.36-2.90 (2H, ring-CH_2 from HT and non-HT-coupling coupling), 6.92-7.12 (1H, ring proton). The ratio of regioregular to regiorandom couplings is 1:1, which is estimated by the relative integration of the HT couplings (δ = 2.79 ppm) and non-HT couplings (δ = 2.55 ppm). Samples are dissolved in deuterated chloroform ($CDCl_3$), and the NMR chemical shifts (δ) are reported in ppm with reference to residual protons of $CDCl_3$ (δ 7.26 ppm in ^{1}H NMR).

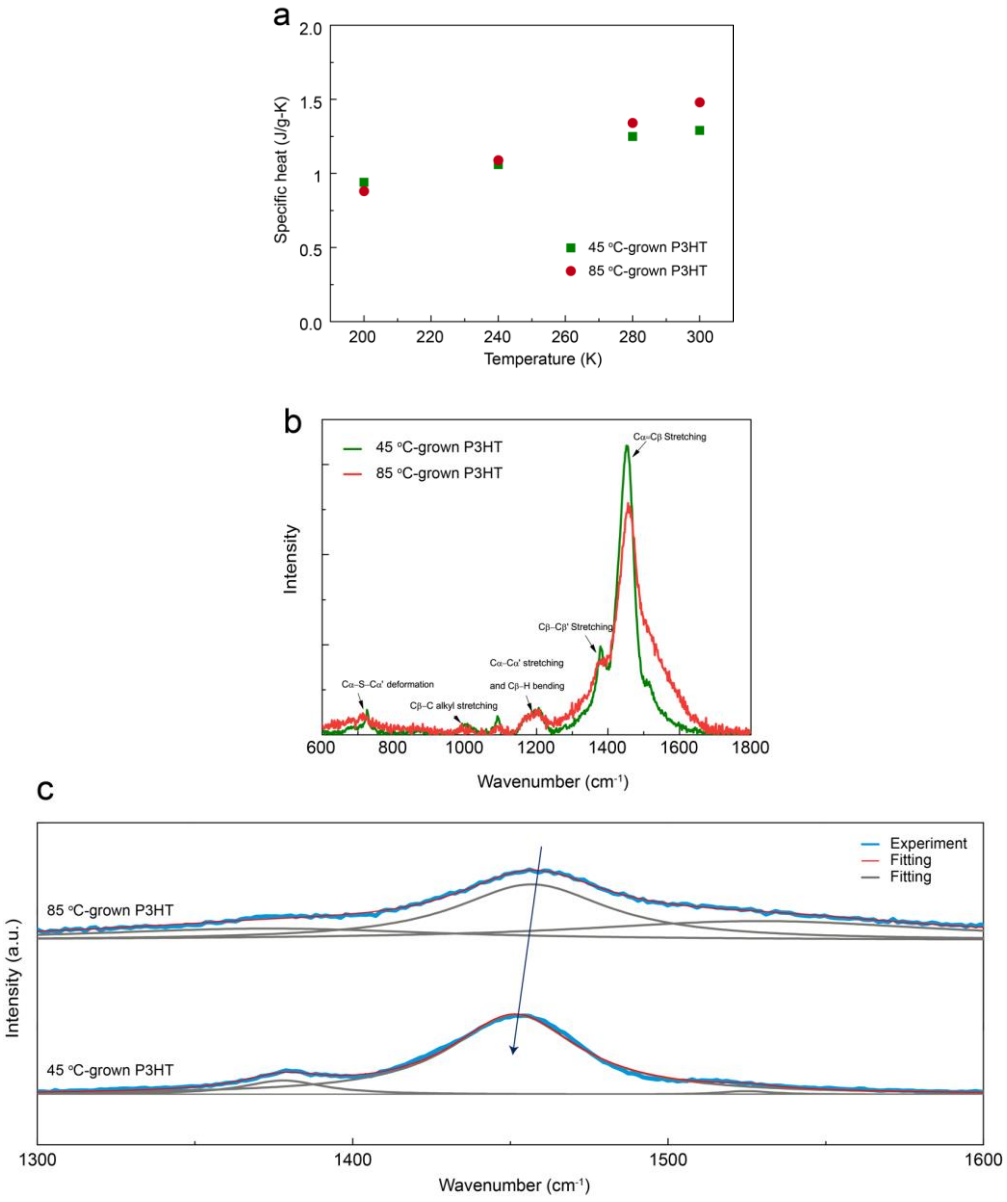

fig. S5. Specific heat analysis and Raman spectroscopy. (**a**) Specific heat results for both 45°C and 85°C-grown P3HT. (**b-c**) Raman spectra of 45°C and 85°C-grown P3HT on glass substrates (*31*). (b) The band at ~1450 cm^{-1} is C_α=C_β bond in the aromatic thiophene ring, and it is associated with neutral conjugated polythiophene segments; the weak shoulder at ~1375 cm^{-1} is assigned to the C_β-$C_{\beta'}$ vibration in the thiophene ring; the band at ~1222 cm^{-1} is assigned to the vibration of the C_α-$C_{\alpha'}$ linkage between adjacent thiophene rings; and ~740 cm^{-1} is assigned to ring deformation. (c) The ordered phase with respect to its disordered phase is identified by a narrower full width at half maximum of the C_α=C_β mode. Compared to the 85°C-grown P3HT, the shift of the C_α=C_β band toward lower wavenumber in 45°C-grown P3HT. This is indicative of a higher conjugation length in 45°C-grown sample, which agrees with UV-vis results.

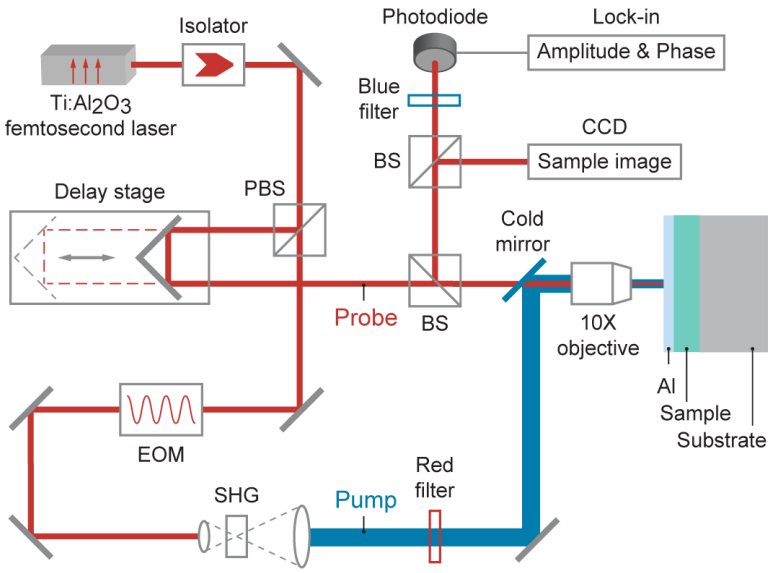

fig. S6. Schematic of the TDTR method for thermal conductivity measurement. The red beam represents the 800 nm output from the Ti-Sapphire laser which ultimately serves as the probe, while the blue path indicates the frequency-doubled 400 nm pump beam.

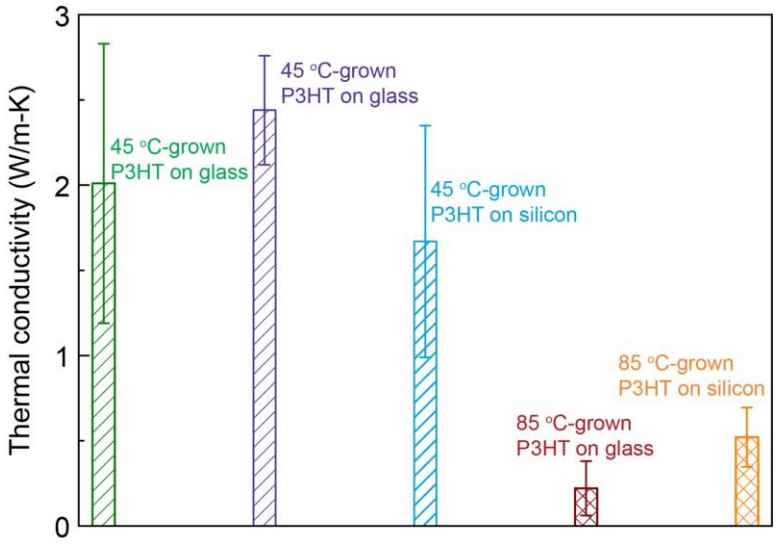

fig. S7. Measured thermal conductivity for multiple samples at 300 K. The bar chart depicts the thermal conductivity for samples from different batches. The error bars represent 95% confidence interval. Samples were grown on different substrates including glass and silicon. The 45°C-grown samples have larger thermal conductivity than the 85°C-grown sample.

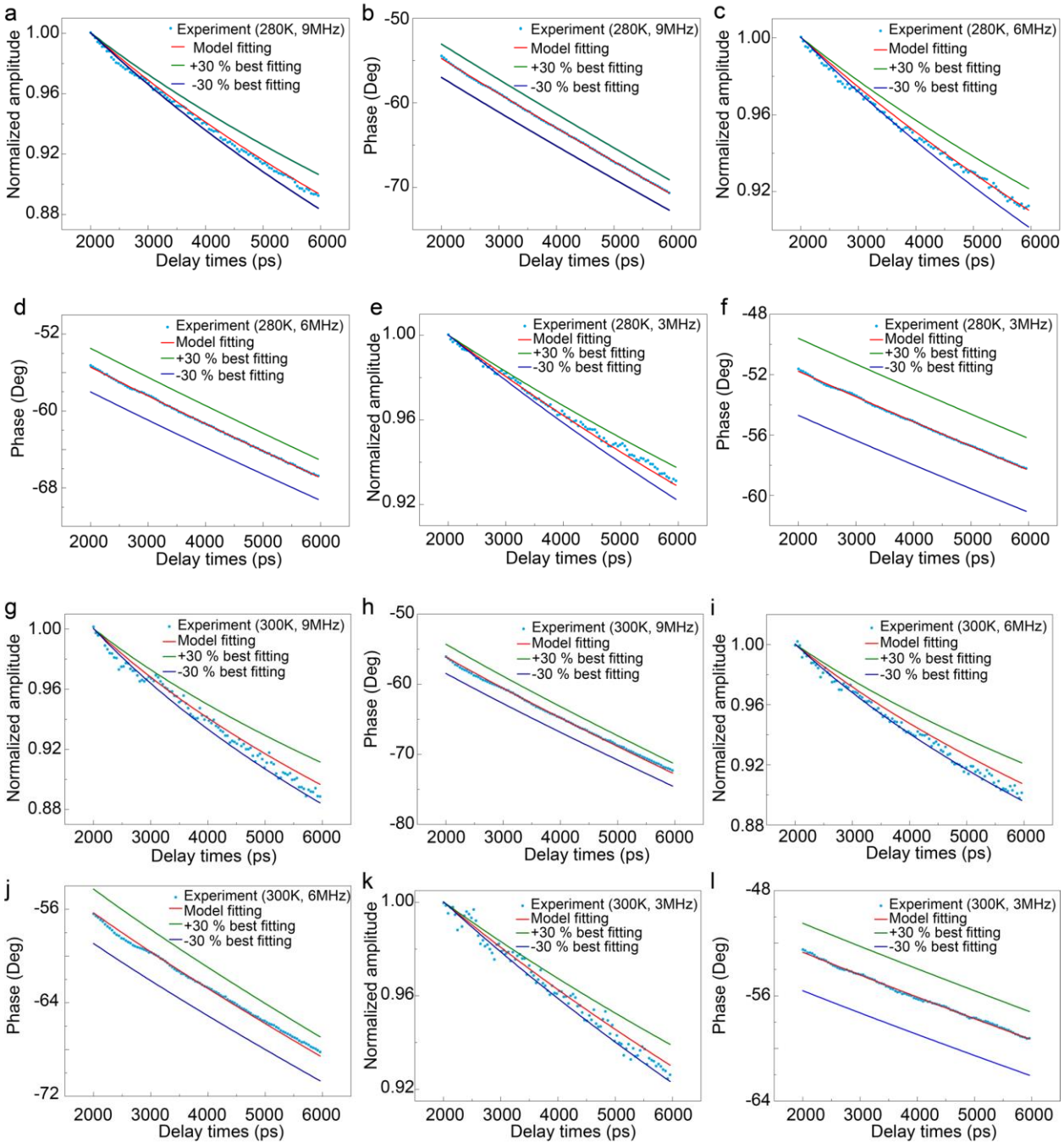

fig. S8. Temperature-dependent TDTR data. Raw data for the amplitude and phase signal along with the fitting result for the 45°C-grown P3HT on glass substrate at both 280 K and 300 K, and at three different modulation frequencies (3 MHz, 6 MHz, and 9 MHz). We note that the best fit for the thermal conductivity agrees well with the phase as well as amplitude signal across the delay time, while a different value for the thermal conductivity leads to significant deviation from the measurement curve.

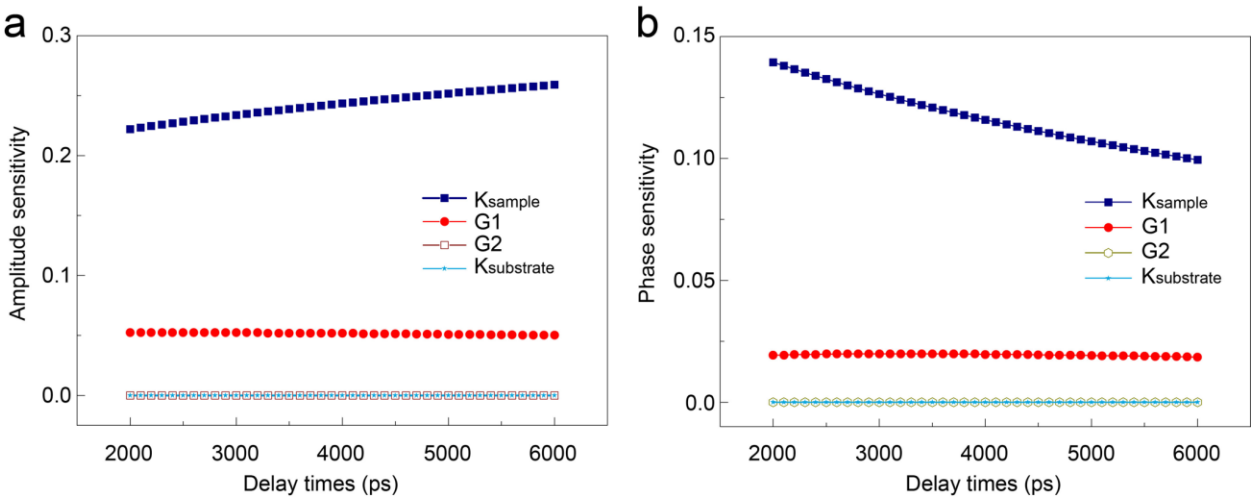

fig. S9. TDTR sensitivity analysis. (**a**) Amplitude signal and (**b**) phase signal for 45°C-grown P3HT at 300 K (modulation frequency 3 MHz). For this representative analysis, we employed a five-layer model which includes the effect from the substrate. We have chosen the substrate to be glass (thermal conductivity $k_{substrate}$ = 1.2 W/m-K), and the sample thermal conductivity (k_{sample}) to be 2 W/m-K. The interface conductance between aluminum and sample (G1) is taken to be 7×10^7 W/m^2-K, while the interface conductance between sample and substrate (G2) is assumed at 10^8 W/m^2-K. The sample thickness is ~160 nm on the glass substrate, and the aluminum thickness is taken to be 107 nm.

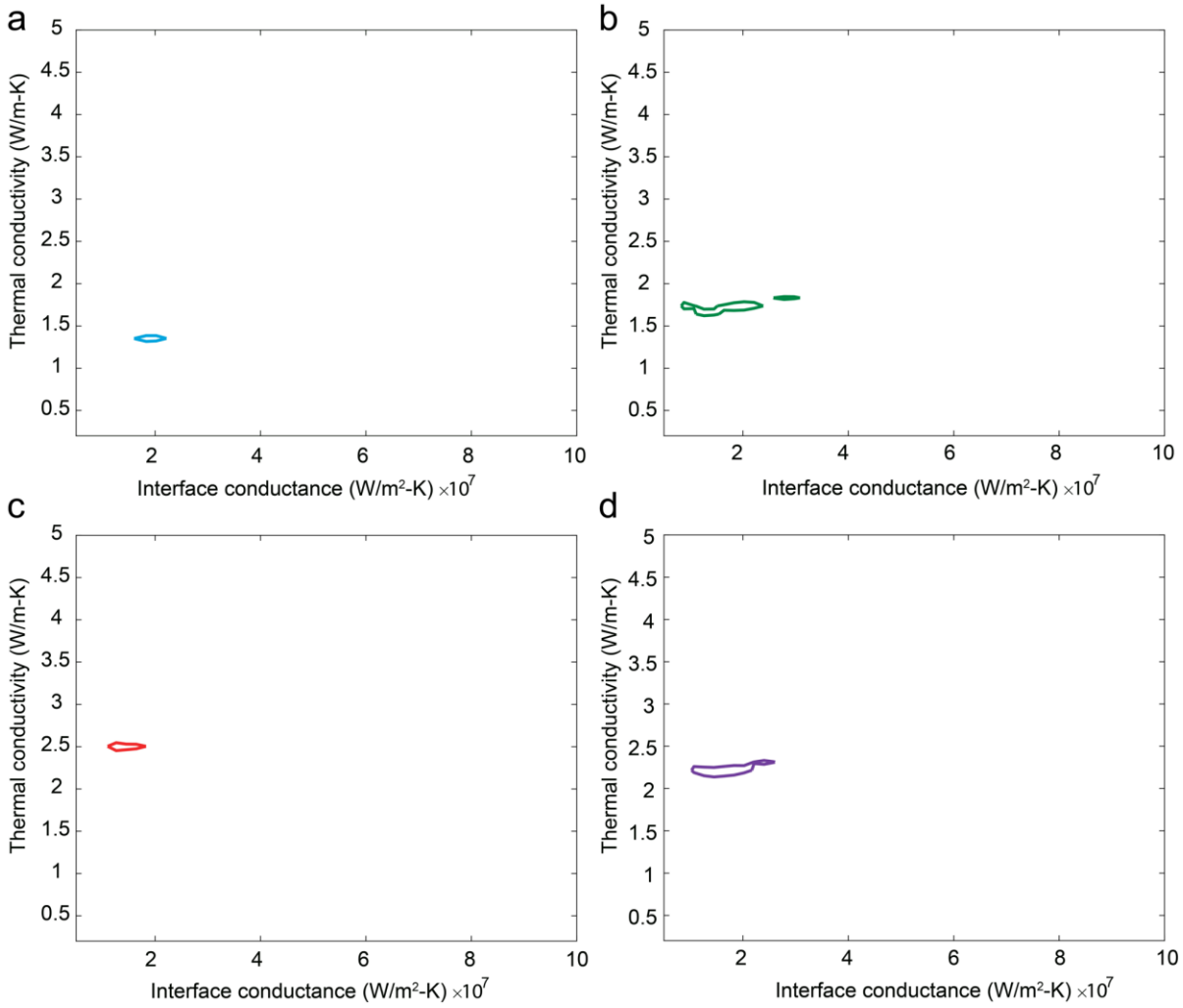

fig. S10. TDTR uncertainty analysis. Residual contour plot with respect to sample thermal conductivity and thermal interface conductance for the 45°C-grown P3HT, at four different temperatures: (**a**) 200 K, (**b**) 240 K, (**c**) 280 K, and (**d**) 300 K. Data measured at a modulation frequency of 3 MHz is used for this study.